

Inclusion of Building-Resolving Capabilities Into the FastEddy® GPU-LES Model Using an Immersed Body Force Method

Muñoz-Esparza, Domingo; Sauer, Jeremy A.; Shin, Hyeyum Hailey; Sharman, Robert; Kosović, Branko; Meech, Scott; García-Sánchez, Clara; Steiner, Matthias; Knievel, Jason; Pinto, James

DOI

[10.1029/2020MS002141](https://doi.org/10.1029/2020MS002141)

Publication date

2020

Document Version

Final published version

Published in

Journal of Advances in Modeling Earth Systems

Citation (APA)

Muñoz-Esparza, D., Sauer, J. A., Shin, H. H., Sharman, R., Kosović, B., Meech, S., García-Sánchez, C., Steiner, M., Knievel, J., Pinto, J., & Swerdlin, S. (2020). Inclusion of Building-Resolving Capabilities Into the FastEddy® GPU-LES Model Using an Immersed Body Force Method. *Journal of Advances in Modeling Earth Systems*, 12(11), Article e2020MS002141. <https://doi.org/10.1029/2020MS002141>

Important note

To cite this publication, please use the final published version (if applicable).
Please check the document version above.

Copyright

Other than for strictly personal use, it is not permitted to download, forward or distribute the text or part of it, without the consent of the author(s) and/or copyright holder(s), unless the work is under an open content license such as Creative Commons.

Takedown policy

Please contact us and provide details if you believe this document breaches copyrights.
We will remove access to the work immediately and investigate your claim.



RESEARCH ARTICLE

10.1029/2020MS002141

Inclusion of Building-Resolving Capabilities Into the FastEddy® GPU-LES Model Using an Immersed Body Force Method

Key Points:

- An immersed body force method (IBFM) is implemented in the FastEddy model for explicit representation of building effects
- The IBFM is extended to be scale independent and to control building surface temperatures
- The IBFM is validated with observations at laboratory and atmospheric scales

Domingo Muñoz-Esparza¹ , Jeremy A. Sauer¹ , Hyeyum Hailey Shin¹, Robert Sharman¹ , Branko Kosović¹ , Scott Meech¹, Clara García-Sánchez², Matthias Steiner¹ , Jason Knievel¹, James Pinto¹ , and Scott Swerdlin¹

¹National Center for Atmospheric Research, Boulder, CO, USA, ²Faculty of Architecture and the Build Environment, Delft University of Technology, Delft, Netherlands

Correspondence to:

D. Muñoz-Esparza,
domingom@ucar.edu

Citation:

Muñoz-Esparza, D., Sauer, J. A., Shin, H. H., Sharman, R., Kosović, B., Meech, S., et al. (2020). Inclusion of building-resolving capabilities into the FastEddy® GPU-LES model using an immersed body force method. *Journal of Advances in Modeling Earth Systems*, 12, e2020MS002141. <https://doi.org/10.1029/2020MS002141>

Received 14 APR 2020

Accepted 7 OCT 2020

Accepted article online 30 OCT 2020

Abstract As a first step toward achieving full physics urban weather simulation capabilities within the resident-GPU large-eddy simulation (LES) FastEddy® model, we have implemented and verified/validated a method for explicit representation of building effects. Herein, we extend the immersed body force method (IBFM) from Chan and Leach (2007, <https://doi.org/10.1175/2006JAMC1321.1>) to (i) be scale independent and (ii) control building surface temperatures. Through a specific drag-like term in the momentum equations, the IBFM is able to enforce essentially zero velocities within the buildings, in turn resulting in a no-slip boundary condition at the building walls. In addition, we propose similar forcing terms in the energy and mass conservation equations that allow an accurate prescription of the building temperature. The extended IBFM is computationally efficient and has the potential to be coupled to building energy models. The IBFM exhibits excellent agreement with laboratory experiments of an array of staggered cubes at a grid spacing of $\Delta = 1$ mm, demonstrating the applicability of the method beyond the atmospheric scale. In addition, the IBFM is validated at atmospheric scale through simulations of downtown Oklahoma City ($\Delta = 2$ m) using data collected during the Joint Urban 2003 (JU03) field campaign. Our LES IBFM results for mean wind speed, turbulence kinetic energy, and SF₆ transport and dispersion compare well to observations and produce turbulence spectra that are in good agreement with sonic anemometer data. Statistical performance metrics for the JU03 simulations are within the range of other LES models in the literature.

Plain Language Summary A significant majority of social and economic activities are logically concentrated around densely populated urban areas. Consequently, accurate modeling and prediction of urban-scale weather entails a tremendous benefit to society in many ways. Herein, we extend the immersed body force method (IBFM), which allows explicit representation of building effects in microscale numerical models, to be applicable to disparate scales and to effectively control building surface temperatures. This computationally efficient method is implemented into the GPU-accelerated large-eddy simulation (LES) FastEddy® model, with the purpose of facilitating a path toward realistic street-scale operational weather forecasting in the near future. We validate the extended IBFM with observations at laboratory scale and urban-scale field measurements over downtown Oklahoma City during the Joint Urban 2003 field campaign. Our LES IBFM results for mean wind speed, turbulence kinetic energy, and SF₆ transport and dispersion compare well to observations, and the corresponding statistical performance metrics are within the range of other LES models in the literature employing body fitted and immersed boundary approaches.

1. Introduction

A significant majority of social and economic activities are logically concentrated around densely populated urban areas. Consequently, accurate modeling and prediction of urban-scale weather entails a tremendous benefit to the society in many ways. However, there exist significant challenges associated with the influence and nature of small scale heterogeneities within the urban landscape that govern critical aspects of flow patterns and microclimates in cities. Explicit representation of urban microscale features does require very fine grid spacings, $\Delta \sim 10^{-1} - 10^1$ m, typically preventing building-resolving simulations from being routinely carried out with microscale models due to the nearly prohibitive high-performance computing resources

©2020. The Authors.

This is an open access article under the terms of the Creative Commons Attribution-NonCommercial-NoDerivs License, which permits use and distribution in any medium, provided the original work is properly cited, the use is non-commercial and no modifications or adaptations are made.

required. As a result, building-resolving simulations have been thus far restricted primarily to exploratory fundamental research efforts (e.g., Auguste et al., 2019; Chan & Leach, 2007; Cheng & Porté-Agel, 2015; García-Sánchez et al., 2018; Jiang et al., 2017; Kanda, 2006; Lee et al., 2019; Lundquist et al., 2012; Park et al., 2015; Smolarkiewicz et al., 2007; Tomas et al., 2016; Wyszogrodzki et al., 2012).

An attractive method for making these high-fidelity microscale urban weather simulations computationally efficient and more affordable on a routine basis, is the use of accelerated Graphic Processing Unit (GPU) architectures. The potential of this accelerated computing paradigm has resulted in the recent emergence of a handful of microscale codes that are either resident-GPU or hybrid CPU-GPU microscale atmospheric solvers (Lenz et al., 2019; Maronga et al., 2015; Schalkwijk et al., 2012; Thibault & Senocak, 2009; van Heerwaarden et al., 2017). In that regard, a novel resident-GPU large-eddy simulation (LES) model for the study of atmospheric boundary layer (ABL) phenomena: FastEddy[®] (hereafter referred to as FastEddy), was recently introduced. Model formulation and implementation details of FastEddy are described in Sauer and Muñoz-Esparza (2020), together with a suite of validation cases including canonical ABL flows for different atmospheric stabilities and flow over complex terrain. FastEddy has proven to be highly efficient, demonstrating performance speed up of 1 GPU matching 256 CPU cores (6 times faster prediction rate under equivalent power or 8 times lower power consumption at an equivalent CPU/GPU prediction rate). Herein, we extend the capabilities of FastEddy to include explicit representation of buildings. Our objective is to provide a highly efficient and accurate model to study flow, transport and exchanges in the urban environment, achieved by modeling microscale atmospheric phenomena within the urban canopy and its interaction with the ABL.

There exist two main approaches to represent building effects in numerical models. The traditional approach, coming from the computational fluid dynamics (CFD) community, is to represent buildings as boundaries of the computational domain (solid boundaries), shaped to account for the building layout (e.g., Blocken, 2018). Typically, grid refinement is used with body fitted grids near the building boundaries, either using structured conformal grids (e.g., Gorré et al., 2010), or unstructured meshes to avoid placing a high density of grid points in regions away from building walls (e.g., García-Sánchez et al., 2018). Nevertheless, this type of grid refinement imposes sudden changes in the filter width of LES, specially in the case of implicit filtering where the grid dictates the filter width. This grid distribution can result in significant gradients within the eddy diffusivity field, leading to energy pileups (Vanella et al., 2008). Also, it has been shown by Mirocha et al. (2013) and Muñoz-Esparza, Kosović, García-Sánchez, and van Beeck (2014) that small scales consistent with the grid size are not generated instantaneously in LES when the grid is suddenly refined. Thus, the turbulent response of the flow to the embedded obstacles will not be fully represented in the vicinity of buildings when using localized grid refinements. In addition, body-fitted grids have the disadvantage of being complex and requiring significant time to be designed. However, grid refinement can be advantageous when the aim is to resolve the near-wall region.

The other main approach to represent buildings in numerical models is the immersed boundary method (IBM). This method employs specific forcing terms in the momentum equations to reproduce the behavior of solid walls and that enables using regular grids that do not need to adapt to the geometry of interest (e.g., Iaccarino & Verzicco, 2003; Mittal & Iaccarino, 2005). The IBM has the advantage of not requiring refined grids, and therefore maintains the accuracy and efficiency of uniform discretizations while not suffering from the issues associated with grid changes in LES modeling previously mentioned. In the context of atmospheric flow models, the use of the IBM has gained significant popularity in the last several years, both for terrain and building representations (e.g., Anderson, 2013; Bao et al., 2018; Jähn et al., 2016; Letzel et al., 2008; Lundquist et al., 2012; Senocak et al., 2004). An alternative approach to the IBM was introduced by Chan and Leach (2007). In their method, the authors used drag terms (body forces) in the momentum equations in a similar fashion to canopy models. By using a sufficiently large drag coefficient at all of the immersed grid points corresponding to a building, the flow acts as encountering a solid obstacle. Contemporaneously, an equivalent method was independently proposed by Smolarkiewicz et al. (2007). In essence, that method seeks the same effect, but with the significant slow down of the fluid within the immersed body achieved through a momentum tendency that is proportional to the velocity over a time scale.

The body force method shares the same advantages of the IBM, that is, it allows uniform grids and therefore has reduced numerical errors (e.g., Iaccarino & Verzicco, 2003), and in addition, does not require application of an interpolation scheme to impose a specific boundary condition at the immersed boundary. Moreover,

it is computationally more efficient than IBM since it does not require any interpolation operations to be performed, and therefore fits well within our GPU-accelerated modeling framework in FastEddy. In addition, given its similarity to a canopy formulation, it has potential to be extended to represent effects from grid-resolved vegetation elements like bushes and trees. However, predicted results in the vicinity of the immersed buildings are, as expected, slightly less accurate. Herein, we propose an extension to the method from Chan and Leach (2007) that permits scale-independent application (i.e., can be seamlessly applied from laboratory to urban scales) and allows controlled heat exchange between buildings and the environment. The adequacy of this method is demonstrated by employing an isolated building configuration. Further validation of this immersed body force method is presented using two test cases for which observations are available, one corresponding to laboratory scale and the other to an urban scenario at atmospheric scale.

2. Immersed Body Force Method for Building Representation and Large-Eddy Simulation Model Formulation

The method from Chan and Leach (2007), hereafter referred to as the immersed body force method (IBFM), is based upon the application of forcing terms to the momentum equations that have the following form

$$F_{u_i} = -C_d \bar{\rho} |\tilde{u}_i| \tilde{u}_i, \quad (1)$$

where u_i is the component of the velocity field in the $i, j, k = 1, 2, 3$ directions for zonal, meridional, and vertical, respectively, and ρ is the air density. The minus sign imposes a flow deceleration from the building unaware solution, which becomes essentially 0 provided a sufficiently large drag coefficient, C_d . Chan and Leach (2007) looked into the accuracy of the IBFM depending on the amplitude of the drag coefficient, $C_d = 15, 50, 100 \text{ m}^{-1}$. From these three values, the authors found that $C_d = 100 \text{ m}^{-1}$ resulted in a flow solution (wind speed and air patterns) that was very close to the reference simulation using solid boundaries (often termed the CFD approach). The method was conceived as an efficient way to tackle emergency response dispersion simulations, for which the airflow in the street canyons needs to be fairly well resolved but the affordable grid spacing is relatively coarse.

One aspect that requires special attention in the IBFM formulation is the magnitude of C_d . The drag coefficient, as already mentioned, has units of m^{-1} . Comparison of Equation 1 to typical canopy parameterizations reveals that C_d is not a standard drag coefficient but rather represents the product of the drag coefficient (C'_d , nondimensional) and the plant area density (A_p , m^{-1} , typically a function of height), when compared to canopy drag formulations (Yamada, 1982): $C_d = C'_d A_p$. The use of a constant C_d , as proposed by Chan and Leach (2007), neglects the influence of the grid spacing on A_p , and in turn on the magnitude of the imposed drag force. Early implementation and testing of the IBFM confirmed the lack of a constant C_d that is valid across a wide range of grid sizes. To overcome that limitation, we propose a scale-independent C_d formulation that accounts for the grid size and can therefore be used to model solid obstacles at any scale (from laboratory to atmosphere).

In order to find a more general expression for C_d , we compare the body force from Equation 1 to the advection term in the Navier-Stokes equations

$$C_d \bar{\rho} |\tilde{u}_i| \tilde{u}_i \sim \frac{\partial \bar{\rho} \tilde{u}_i \tilde{u}_j}{\partial x_j} \rightarrow C_d = \alpha_m \beta_r \Delta^{-1}, \quad (2)$$

where Δ is the nominal grid size ($= \sqrt[3]{\Delta x \Delta y \Delta z}$) and α_m is a constant coefficient. In order to determine the value of α_m , we invoke the following arguments: (i) The drag force is dominant over the advection term, $\mathcal{O}(10)$, and (ii) the spatial gradient of the squared velocity field is much larger than the velocity field itself, especially at air-obstacle interfaces, $\Delta u_i u_j \gg u_i^2$, $\mathcal{O}(10^2)$. As a result, we propose $\alpha_m = 10^3$, and therefore $C_d = 10^3 \beta_r \Delta^{-1}$. Lower values of α_m were found to progressively allow more air to flow through the immersed bodies, while larger values resulted in numerical instabilities. Such value of α_m leads to a drag coefficient of $C_d = 100\text{--}1,000$ for $\Delta = 1\text{--}10$ m, which is consistent with the value of 100 used by Chan and Leach (2007). However, note that when smaller grid sizes are used, as is the case for laboratory scale setups, the term Δ^{-1} compensates for the fact that spatial derivatives become larger, effectively increasing the magnitude of C_d . Finally, the parameter β_r in Equation 2 represents the ratio of volume in a cell occupied by the immersed body (i.e., $\beta_r = 1.0$ for fully immersed cells, $\beta_r = 0.0$ for fluid cells, and $0.0 < \beta_r < 1.0$ for partially intersected bodies).

While the IBFM brings the velocity inside the immersed bodies to essentially 0, there is always a small error that induces some leakage of air flow into the immersed body (also including diffusive effects). This leakage contributes to the homogenization of the temperature field across the interface between the immersed body and the surrounding air. This inherent aspect to the IBFM complicates the application of thermal boundary conditions on immersed bodies that will lead to specific buoyancy effects on the flow field. To rectify this issue, we propose to apply a similar term to Equation 1 to the potential temperature (energy) equation, in order to damp temperature variations toward a specified reference temperature, θ_{ref} ,

$$F_{\theta} = -C_t |U_s| [\bar{\rho}\tilde{\theta} - (\rho\theta)_{ref}], \quad (3)$$

$$F_{\rho} = -C_t |U_s| (\bar{\rho} - \rho_{ref}). \quad (4)$$

Note that a forcing term (Equation 4) was also introduced to the equation of conservation of mass. This term arises from the flux conservative and fully compressible nature of our large-eddy simulation model formulation, within which temperature changes directly affect density. A velocity scale of $U_s = 1 \text{ m s}^{-1}$ is used in Equations 3 and 4 to be unit-consistent. In contrast to Equation 1, the IBFM terms in the energy and mass equations do not depend on the actual velocity field, \tilde{u}_i , rather employing a constant velocity scale. This is done to remove the influence of the velocities within the immersed body from the temperature forcing term, since this would otherwise result in a reduced ability to control and correct temperature departures from the reference target temperature as a zero velocity is approached. Similar analysis to that used for the momentum equation was carried out for the transport equations for density and potential temperature, leading to $\alpha_t = 10$, and employing a scale-independent generalization in a similar fashion as for the momentum term (Equation 2), that is, $C_t = \alpha_t \beta_r \Delta^{-1}$.

The IBFM following Equations 1,3, and 4 was implemented within FastEddy. The continuous governing equations read as follows, where the tilde denotes an Favre filtered quantity ($\tilde{\phi} = \overline{\rho\phi}/\bar{\rho}$), and with the filter implicitly arising from the Taylor series truncation errors inherent to the discretization of the advection operator by finite differencing

$$\frac{\partial \bar{\rho}}{\partial t} = -\frac{\partial \bar{\rho}\tilde{u}_j}{\partial x_j} + F_{\rho}, \quad (5)$$

$$\frac{\partial \bar{\rho}\tilde{u}_i}{\partial t} = -\frac{\partial \bar{\rho}\tilde{u}_i\tilde{u}_j}{\partial x_j} - \frac{\partial \bar{p}'}{\partial x_i} - g\bar{\rho}'\delta_{i,3} - 2\bar{\rho}\epsilon_{ijk}\Omega_j(\tilde{u}_k) - \frac{\partial \tau_{ij}}{\partial x_j} + \nu \frac{\partial^2 \bar{\rho}\tilde{u}_i}{\partial x_j^2} + F_{u_i}, \quad (6)$$

$$\frac{\partial \bar{\rho}\tilde{\theta}}{\partial t} = -\frac{\partial \bar{\rho}\tilde{\theta}\tilde{u}_j}{\partial x_j} - \frac{\partial \tau_{\theta j}}{\partial x_j} + \nu Pr^{-1} \frac{\partial^2 \bar{\rho}\tilde{\theta}}{\partial x_j^2} + F_{\theta}. \quad (7)$$

Here, θ is the potential temperature, defined as $\theta = T(p_0/p)^{R/c_p}$, where T and p are the air temperature and air pressure of the differential volume. The reference pressure is p_0 , R is the ideal gas constant, and c_p is the specific heat of dry air at constant pressure. A nonhydrostatic formulation for momentum conservation is used for atmospheric LES by defining a perturbation pressure, $p' = p - p_H$ and a perturbation density $\rho' = \rho - \rho_H$ as departures from a given hydrostatic base state. Under this formulation, the pressure gradient and buoyancy terms on the right hand side of Equation 6 permit increased precision by tracking the relatively small magnitude perturbations as opposed to total fluctuations that are dominated almost entirely by the hydrostatic part. Momentum conservation in Equation 6 includes Coriolis effects for atmospheric boundary layer (ABL) cases, and where $\Omega_j(\tilde{u}_k)$ is the angular velocity vector of the Earth. Subgrid-scale diffusion, τ_{ij} and $\tau_{\theta j}$, is parameterized using a Smagorinsky-Lilly closure for three-dimensional isotropic turbulence (Lilly, 1966, 1967), with a diagnostic equation for subgrid-scale turbulence kinetic energy (TKE) that assumes equilibrium between production and dissipation (e.g., Muñoz-Esparza et al., 2014). The symbol ν represents the molecular viscosity of the air, and the terms where it appears are neglected for ABL flows under the high-Reynolds number assumption, and with Pr being the Prandtl number. Finally, the F right-hand-side terms account for the additional forcing terms required to represent other physics parameterizations, such as the IBFM. For all the results presented herein, a fifth-order scheme was employed for spatial discretization of the advection operator (Wicker & Skamarock, 2002), while a third-order explicit Runge-Kutta method is used for time integration. The rest of spatial gradients as required for the SGS diffusion and pressure terms are discretized using second-order centered differences.

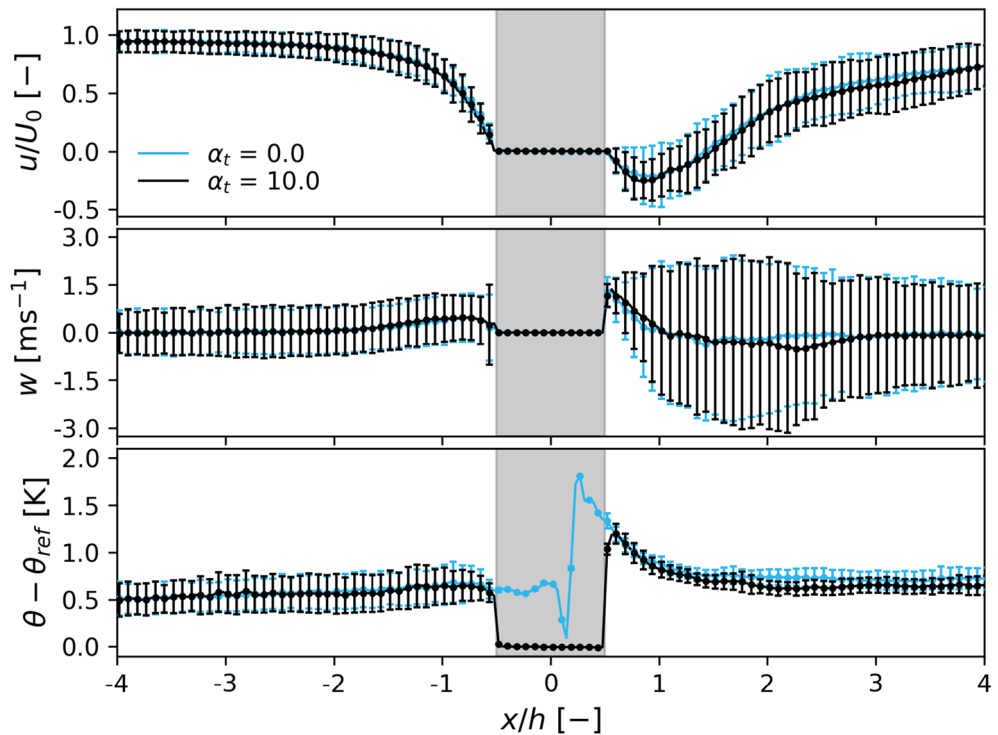


Figure 1. Streamwise evolution of streamwise velocity, u/U_0 , vertical velocity, w , and potential temperature, θ , at $z/h = 0.5$ for the original IBFM ($\alpha_t = 0.0$) and our extended IBFM that includes control of thermal effects ($\alpha_t = 10.0$). The error bars represent one standard deviation, and the gray shaded region denotes the building of size h .

Verification of the IBFM implementation is first presented using a simple setup. The case consists of an isolated cubical building of height $h = 120$ m. The domain extent is $L_x, L_y, L_z = 24h, 12h, 10h$, in the streamwise, spanwise and vertical directions, respectively, with a uniform grid spacing of $\Delta = 5$ m. Lateral boundary conditions were imposed through mean profiles of the prognostic variables derived from a precursor run using periodic lateral boundary conditions, which included Coriolis effects but did not include the building. The flow is driven by a geostrophic wind in the x direction that is constant with height, $U_g = 10$ m s⁻¹, and an initial boundary layer height of $z_i = 400$ m was specified. A three-layer vertical profile of potential temperature was employed, with $\theta = 300$ K for $z \leq z_i$, and a strong capping inversion of $\partial\theta/\partial z = 0.08$ K m⁻¹ above and over a 250-m layer (Δz_{ci}) followed by a weaker stratified layer from $z_i + \Delta z_{ci}$ to the domain top ($=0.003$ K m⁻¹). Roughness length was set to $z_0 = 0.1$ m applied over nonbuilding regions and Coriolis effects were removed (flow is rotated in the streamwise direction).

The resulting solution was horizontally averaged to derive mean vertical profiles of all prognostic variables, followed by a rotation of the horizontal wind speed in the streamwise direction, subsequently applied as boundary conditions at the four lateral boundaries of the limited area domain (LAD), in effect acting as a large-scale pressure gradient driving the flow with the magnitude of our equilibrium winds (and where the Coriolis force is inactive). For the building inclusive simulation, a convective (positive) kinematic heat flux of $\langle w'\theta' \rangle_s = 0.3$ K m s⁻¹ was imposed at the ground (over the building-free extent) to demonstrate the ability of the extended IBFM to handle thermal effects. The building center was placed $13.5h$ from the inflow boundary, and the cell perturbation method (Muñoz-Esparza et al., 2014, 2015) was used to generate fully developed turbulence from the smooth inflow boundary conditions.

The spatial evolutions of streamwise velocity, vertical velocity and potential temperature in the x direction at a height of $z/h = 0.5$ are presented in Figure 1. Comparison of the IBFM method with control of thermal effects ($\alpha_t = 10.0$) to the original implementation ($\alpha_t = 0.0$) results in similar velocity field distributions. In both cases, the streamwise velocity gradually becomes 0 at $x/h > -2$, upstream of the building. On the lee side, a recirculating flow region develops, which progressively recovers with increased downstream distance. The IBFM results in essentially zero mean velocity inside the building for all of the velocity components (velocity residuals 10^{-3} – 10^{-4} m s⁻¹), demonstrating its ability to represent the impact of a solid obstacle on

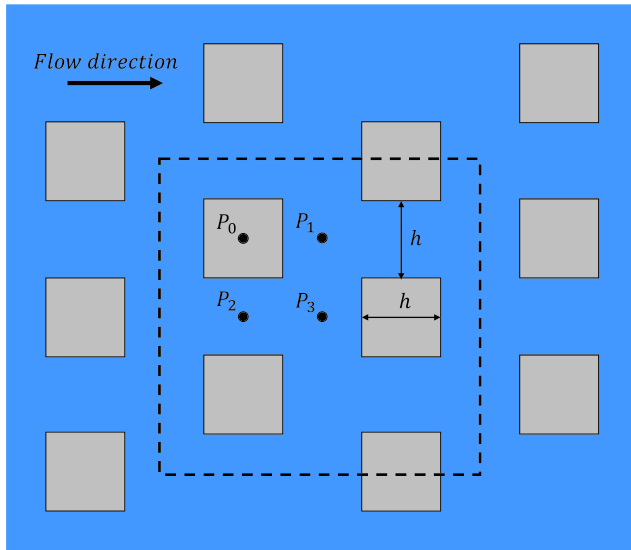


Figure 2. Schematic top view of the staggered array of cubes from the wind tunnel experiment by Castro et al. (2006) used for the laboratory-scale validation of the IBFM. The dashed line denotes the region considered for the numerical modeling domain.

the velocity field. Error bars represent one standard deviation of the particular velocity component. These are omitted within the building given the negligible variance values there (variance of $10^{-6} \text{ m}^2 \text{ s}^{-2}$). The bottom panel in Figure 1 demonstrates how our proposed extension to the IBFM is effective in maintaining the temperature of the building at the prescribed value, $\theta_{ref} = 300 \text{ K}$ (mean error of 10^{-3} K and variance of 10^{-6} – 10^{-8} K^2).

While the overall differences between the thermal extension and the original approach are not significant on the velocity field for this particular case, a few distinct features emerge. As already mentioned, the small leakage of the IBFM (both from advection and diffusion) results in penetration of air warmed by convection inside the building. After 2 h of simulation, the maximum temperature inside the building increases by 1.75 K from the initial condition. In contrast, the IBFM with temperature correction maintains the target temperature accurately. This isothermal condition at the building causes a horizontal cooling heat flux as the surrounding air temperature increases throughout the course of the simulation. The impact of this effect can be seen in the temperature distribution in the lee side of the building, where temperatures are lower on average than for the original IBFM method ($\alpha_t = 0.0$). In the region near the lee side wall of the building, $x/h = 0.5$, the cooling heat flux acts as a turbulence suppression mechanism, observed in the smaller ampli-

tude of the standard deviation of the velocity for $0.5 < x/h < 1.5$, also having some effect on the mean velocity distribution. In the $\alpha_t = 0.0$ case, the temperature at the building wall is larger than that of the surrounding air, in turn inducing a positive heat flux. In addition, a clear signature of this effect is found on the distribution of vertical velocity where the temperature differences are larger ($2.0 < x/h < 3.0$). That temperature difference clearly generates a bias in the mean w toward larger values, as well as a slightly larger u component. These results demonstrate the viability of the extended IBFM to impose a zero velocity condition on the surrounding flow field and to be able to impose the building temperature. The latter is a key aspect when realistic simulation of thermal effects is required, through coupled urban energy balance models, and which plays an important role in the competition of shear-driven and buoyancy-driven turbulence and the resulting flow circulations within an urban canopy (e.g., Li et al., 2016; Park et al., 2012; Yaghoobian et al., 2014).

3. Staggered Array of Cubes at Wind Tunnel Scale

In this section, validation of the IBFM at a laboratory scale is presented. The purpose is twofold: (i) to demonstrate the validity of the scale-independent formulation for C_d and, (ii) to validate the IBFM based on measurements in a controlled environment (this is difficult to accomplish at atmospheric scale, given the predictability issues of weather, as we will discuss in section 4). For this exercise, the wind tunnel experiment from Castro et al. (2006) was selected. The experiment was performed in the EnFlo A wind tunnel at the University of Surrey, and consisted of a series of $h = 20 \text{ mm}$ side cubes arranged in a symmetrical, staggered pattern with an area coverage of 25%. Mean and fluctuating components of the three dimensional velocity field were measured by means of hot-wire and laser doppler anemometry. A schematic of the cube array layout is shown in Figure 2. The wind tunnel experiment included an array of 22×22 cubes. Therefore, it can be assumed that by the time the flow reached the measurement locations, P_{0-3} , a quasi-equilibrium state was achieved. This allows us to simplify our numerical setup due to the repetitive pattern of the array of cubes and impose lateral periodic boundary conditions over the section delimited by the dashed line in Figure 2, significantly reducing the computational burden that would be required to simulate the entire wind tunnel. This is similar to the setup utilized by Tomas et al. (2016), which obtained satisfactory results when compared to the same experimental dataset employed herein.

The computational domain spanned $L_x, L_y, L_z = 4h, 4h, 10h$, in the streamwise, spanwise and vertical directions, respectively, with a uniform grid spacing of $\Delta = 1 \text{ mm}$. An additional forcing term was added to the momentum equation in the x direction to impose a constant pressure gradient in the streamwise direction, $F_{u_1} = \partial p / \partial x = -\rho u_\tau^2 / L_z$, where u_τ is the friction velocity. The friction Reynolds number for the experiment

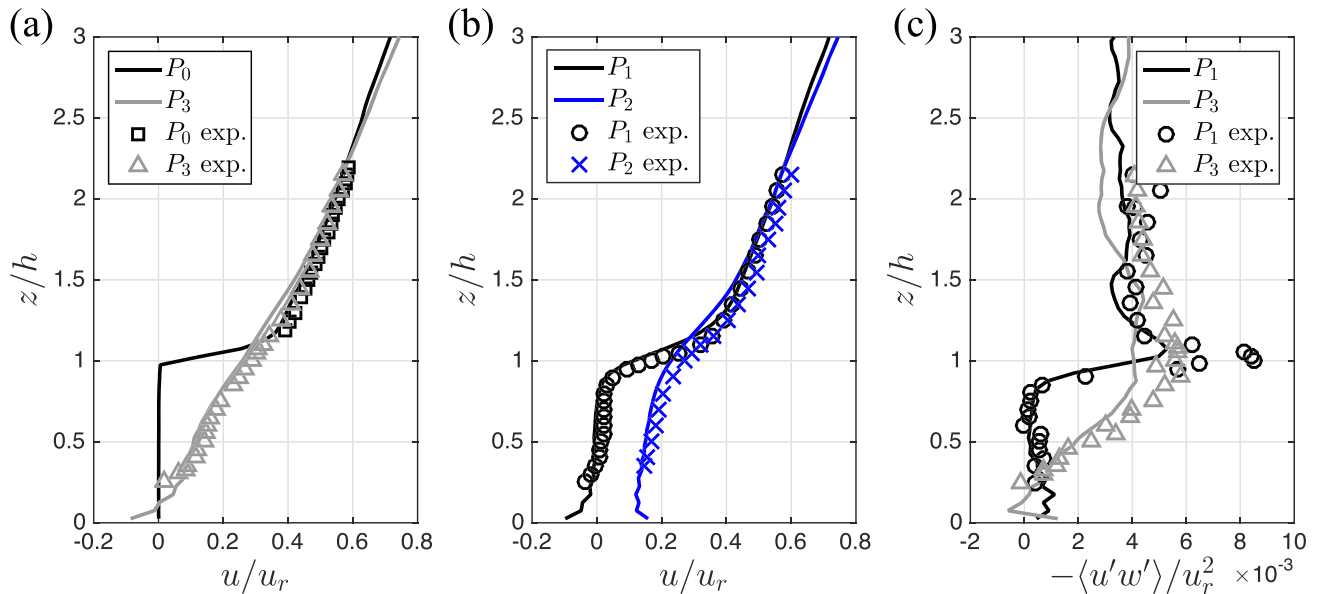


Figure 3. Comparison of velocity (a, b) and momentum flux (c) profiles between the modeling results (solid lines) and the experimental data (symbols) from Castro et al. (2006) at several downstream distances from the center of the cube.

was estimated to be $Re_{r,exp} = u_r h / \nu \approx 1,000$, with $u_r = 0.7 \text{ m s}^{-1}$. In our simulation, $\partial p / \partial x$ was adjusted to match the velocity measured at the farthest distance away from the surface in the experiment. A pressure gradient of $\partial p / \partial x = -3.875 \text{ kg m}^{-2} \text{ s}^{-2}$ was imposed, resulting in $Re_r = 1,216$ and $u_r = 0.817 \text{ m s}^{-1}$, which are in close agreement with the experimental setup values. Viscous terms were considered in Equations 6 and 7 due to the low Reynolds number flow being considered, with a kinematic air viscosity of $\nu = 1.576 \times 10^{-5} \text{ m}^2 \text{ s}^{-1}$ corresponding to $T = 300 \text{ K}$. A no-slip boundary condition was applied at the bottom and top boundaries of the domain.

The eddy turnover time, representative of the largest eddies shed by the cubes is defined as $T = h / u_r$. The simulation was run for an initial $51T$ ($=1.25 \text{ s}$) allowing the flow to equilibrate and adjust from the initial condition to the imposed pressure gradient ($u_r = 10 \text{ m s}^{-1}$, the nominal free stream velocity in the experiments), with a timestep of $\Delta t = 2.5 \times 10^{-6} \text{ s}$. Then, an additional $205T$ were simulated ($=5.0 \text{ s}$, 2 million timesteps), with an output frequency of 1,000 timesteps. The averaging time is sufficiently larger than $50T$, which was found by Coceal et al. (2006) as too short to properly average slowly evolving streamwise circulations in the outer layer, so our results can be regarded as statistically converged. Moreover, the periodic boundary conditions likely result in reduced times required for statistical convergence.

It is worth remarking that when we tested the original version of the IBFM, that is, $C_d = 10^3 \text{ m}^{-1}$, the resulting flow solution did not feel the presence of the surface-mounted cubes. This is due to the fact that spatial derivatives are in this case computed over a grid spacing of $\Delta = 1 \text{ mm}$, which increases the magnitude of gradients by a factor of 1,000 compared to the atmospheric scale. Our experiments at atmospheric scale with $\Delta = 2\text{--}20 \text{ m}$ revealed that no scale correction is required within that range, which is the typical span of urban modeling at atmospheric scale. Therefore, the scale-independent correction is in practical terms applied for $\Delta < 1 \text{ m}$, $C_d = \alpha_m \max(\Delta^{-1}, 1.0)$. However, the scale-independent extension of the IBFM should not be confused with a proper building representation of resolved flow effects irrespective of the utilized grid spacing. In fact, we have looked at this aspect in a separate study and found that in order to resolve building-induced vortex shedding, mean-flow features, and turbulence statistics, at least 6, 10, 12, and 24 grid points per building side with an advection scheme of a minimum of third order are required, respectively (Shin et al., 2020).

Comparison of vertical velocity profiles between the numerical simulation (solid lines) and the wind tunnel experiment (symbols) from Castro et al. (2006) is presented in Figures 3a and 3b. At P_0 , the location at the center of the cube, the IBFM is able to reproduce the targeted zero velocity distribution inside the building ($z/h < 1.0$). The model results are in excellent agreement with the experimental data, realistically

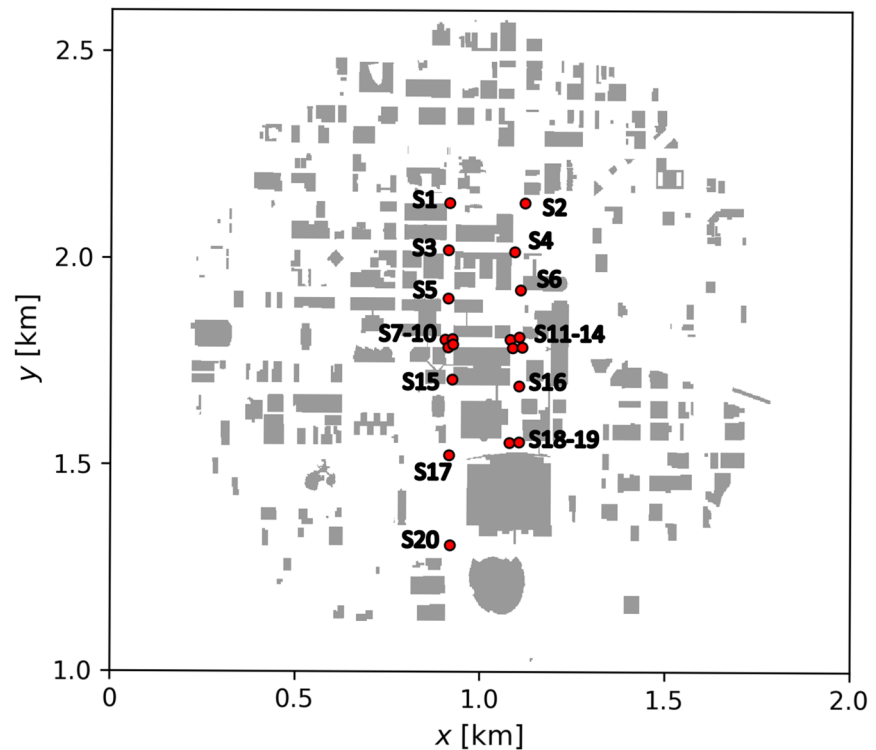


Figure 4. Simulated building layout (gray areas) from downtown Oklahoma City as discretized by the model grid spacing ($\Delta = 2$ m). The red dots denote the location of the twenty 8-m height mounted sonic anemometers (S). The total horizontal domain extent is 2.0×3.0 km², which the coordinates of the plot are referred to.

reproducing the wake recovery from P_1 to P_2 and P_3 . Moreover, the distribution of momentum flux is also in good agreement with the experiments, correctly replicating the observed peak resulting from the shear-layer induced turbulence at P_1 near the cube top and the turbulence redistribution further downstream at P_3 (see Figure 3c). While the momentum flux was slightly underestimated, the distributions are similar to the laser doppler velocimetry measurements. We attribute this discrepancy to the differences in setup with respect to the wind tunnel, which modeled a finite-size array of cubes, as well as uncertainties in the measurement techniques (sensor accuracy and positioning precision). Moreover, our velocity and Reynolds stress distributions obtained with the IBFM are of similar accuracy to those in Tomas et al. (2016) with the IBM and a similar numerical setup to the one employed herein. All these results demonstrate the accuracy of our method to represent flow around obstacles, which will be farther validated at atmospheric scales in the next subsection.

4. Urban Environment Flow, Turbulence, and Dispersion During the Joint Urban 2003 Field Campaign

In order to demonstrate and validate the developed urban modeling framework at atmospheric boundary layer (ABL) scales, we compare to the Joint Urban 2003 (JU03) field experiment. The JU03 campaign took place in Oklahoma City (OKC) during the summer of 2003 (Allwine & Flaherty, 2006). The main purpose of the campaign was to provide quality-assured meteorological and tracer data sets for the validation of indoor and outdoor dispersion models in urban environments. Velocity components, wind directions, and scalar concentrations were measured by sonic anemometers and fast-response tracer gas analyzers, respectively. This campaign represents perhaps the most comprehensive urban field study for which data are publicly available. Due to the number of instruments deployed and the simultaneous measurements of wind, turbulence and tracer concentrations, the dataset has been widely used as reference in the validation of flow and dispersion with both CFD and LES models in urban environments (Chan & Leach, 2007; García-Sánchez et al., 2018; Lundquist et al., 2012; Neophytou et al., 2011; Wiersema et al., 2020; Wyszogrodzki et al., 2012).

During the JU03's intensive observational periods (IOPs), 20 stations were deployed in the downtown central business district (see Figure 4). Each station consisted of a 3-D sonic anemometer sampling the three

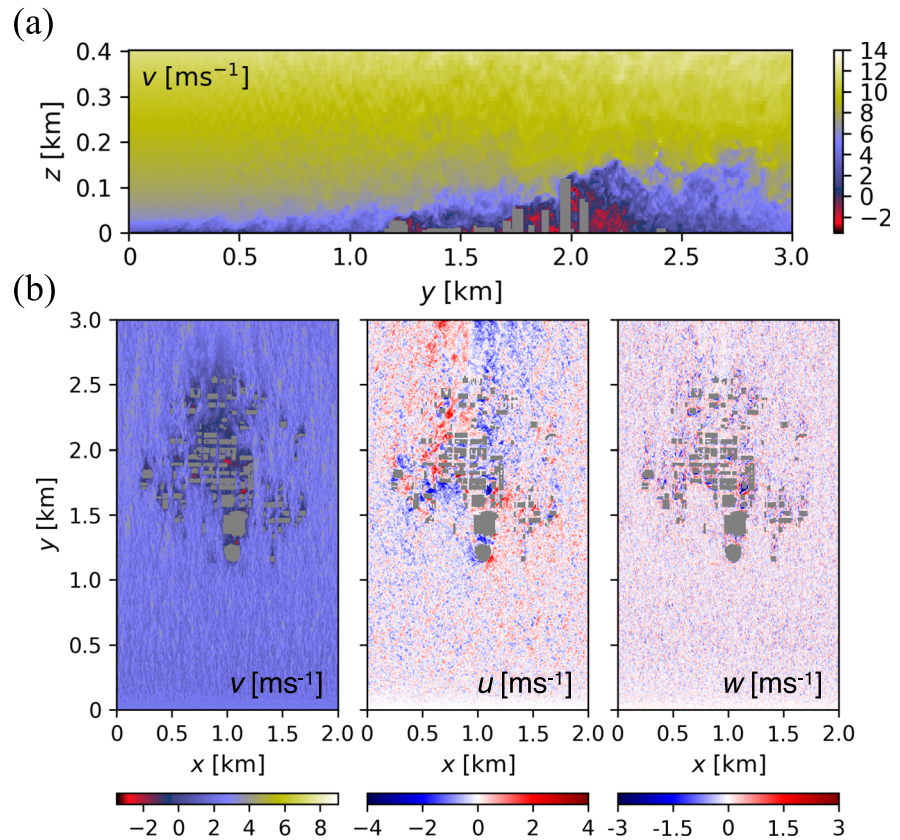


Figure 5. Instantaneous contours of velocity components: v = streamwise, u = spanwise, w = vertical. (a) Vertical cross section of streamwise velocity at $x = 1.0$ km. (b) Horizontal plane at $z = 8$ m. Flow direction is southerly. Horizontal extent is the entire computational domain.

components of the wind at 10 Hz, with an accuracy between 1% rms and 0.05 m s^{-1} . The anemometers were located 8 m above ground and enabled calculation of the mean wind speed, wind direction and turbulence kinetic energy (TKE), which will be used to validate our microscale urban modeling capabilities. In addition, 10 programmable integrating gas samplers (PIGS) with a sampling frequency of 2 Hz and located 2.5 m above ground were available during the IOPs (see Figure 9a). Herein, we selected the same period of IOP9 as García-Sánchez et al. (2018), corresponding to the first half hour of the experiment, and that took place between 0400–0430 UTC on 27 July.

A weather station equipped with a cup and vane anemometer located 30 m above ground and upstream of the high-density observational network ($x = 0.5$ km, $y = 0.25$ km in Figure 4) was utilized to estimate the predominant atmospheric conditions as reference to force our semi-idealized simulations. For the selected time of IOP9, the mean wind speed and direction are $U_{30m} = 6.12 \text{ m s}^{-1}$ and $\phi_{30m} = 172.1^\circ$. A separate simulation using periodic lateral boundary conditions was employed to provide mean vertical profiles of the prognostic variables to be used as lateral boundary conditions after planar averaging. Roughness length was set to $z_0 = 0.29$ m, typical of a suburban terrain and as the predominant land surface class present upstream of downtown OKC. The geostrophic wind was adjusted to $U_g = 13.5 \text{ m s}^{-1}$, with a Coriolis parameter of 35.47°N and an initial capping inversion located at $z_i = 500$ m. For the building resolving OKC reference simulation, lateral boundary conditions were aligned with the southern direction for the reference simulation ($\phi_{BC} = 180^\circ$, which we varied $\pm 15^\circ$ as a sensitivity study). These time-invariant, equilibrium profiles are applied as Dirichlet boundary conditions on all lateral boundaries of the domain, in a similar manner to the one-way nesting technique in atmospheric models. The computational domain had an extent of $L_x, L_y, L_z = 2.0, 3.0,$ and 1.2 km, with a uniform grid spacing in the horizontal, $\Delta_h = 2$ m, and stretching in the vertical following a cubic expansion, $\Delta_v = 2\text{--}24$ m ($\Delta_v < 5$ m for $z < 200$ m). The OKC simulations are run for a total time of 42 min, where the initial 12 min are discarded as model spin-up to flash out the initial condition, and the subsequent time period is used for the calculation of statistics with an output frequency of 1 s.

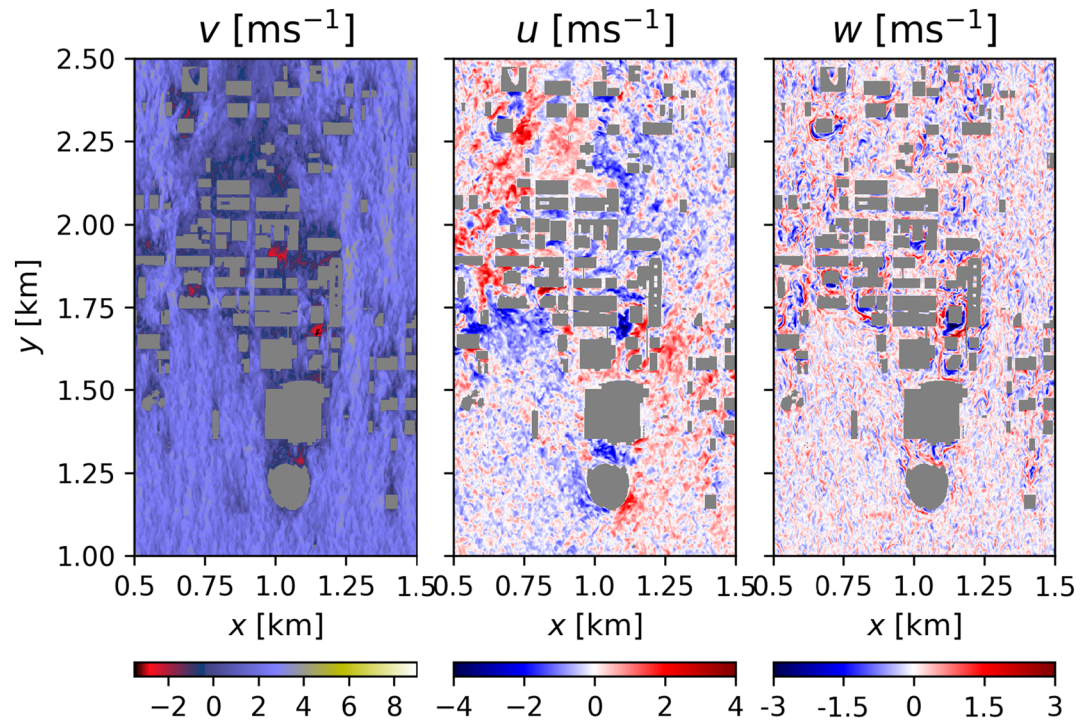


Figure 6. Instantaneous contours of velocity components on a horizontal plane at $z = 8$ m. Same as in Figure 5 but zoomed in over the downtown district of OKC.

Instantaneous contours of the velocity components are presented in Figure 5. These contours show how the application of the cell perturbation method enables a rapid generation of turbulence consistent with the forcing from the smooth horizontally homogeneous lateral boundary conditions. The vertical cross section of streamwise v velocity (Figure 5a) displays the growth of the low momentum at the near-surface region from the building-unaware inflow over the urban environment due to the form drag exerted by the resolved buildings, which also includes instantaneous low velocity ejections penetrating very high in the vertical direction as a consequence of the enhanced turbulence levels. The resulting nature of the imposed drag forces is further evidenced by the velocity contours in a horizontal plane at $z = 8$ m (Figure 5b), exhibiting a systematic deceleration of the incoming wind in the upstream region and lee side of the buildings, as well as a divergent-convergent flow pattern for the city as a whole clearly evidenced from the spanwise u velocity component. A zoomed in view over a portion of the business district of OKC presented in Figure 6 reveals localized strong recirculation regions on the lee side of certain buildings, as well as coherent updraft/downdraft motions as a result of the presence of the buildings and the building-to-building interactions, which is typically associated with strong swirling motions in the horizontal direction. This is a highly unsteady phenomena, as it can be observed in the accompanying animation (<https://doi.org/10.5281/zenodo.4124164>), which shows the complex nature of eddy detachment due to the sharp edges present between building walls in these bluff bodies, and that in addition present a strong spatial variability. These aspects make accurate prediction of flow features within urban canopies extremely challenging for steady state and simplified low-order models.

Assessment of the accuracy of the simulated urban flows and turbulence is performed based on the near-surface observations collected at the sonic anemometer stations deployed during JU03 (Figure 4, $z = 8$ m). Figure 7 shows comparisons of 30-min averaged wind speed, wind direction, and turbulence kinetic energy. Overall, the LES results are in good agreement with the sonic anemometer measurements. Simulated wind speeds are for most of the stations within ± 1 m s⁻¹ of the observations. Interestingly, Stations S7–S10, clustered at the intersection of Robinson and Park Avenues, have the largest errors. We initially hypothesized that this may be in part related to the high density of buildings upstream of that intersection, and likely being more sensitive to uncertainties in boundary conditions. To address that question, we performed two additional simulations in which the lateral boundary conditions were changed to vary the inflow wind direction by $\phi = \pm 15^\circ$ from the reference southerly flow simulation ($\phi = 180^\circ$), also shown in

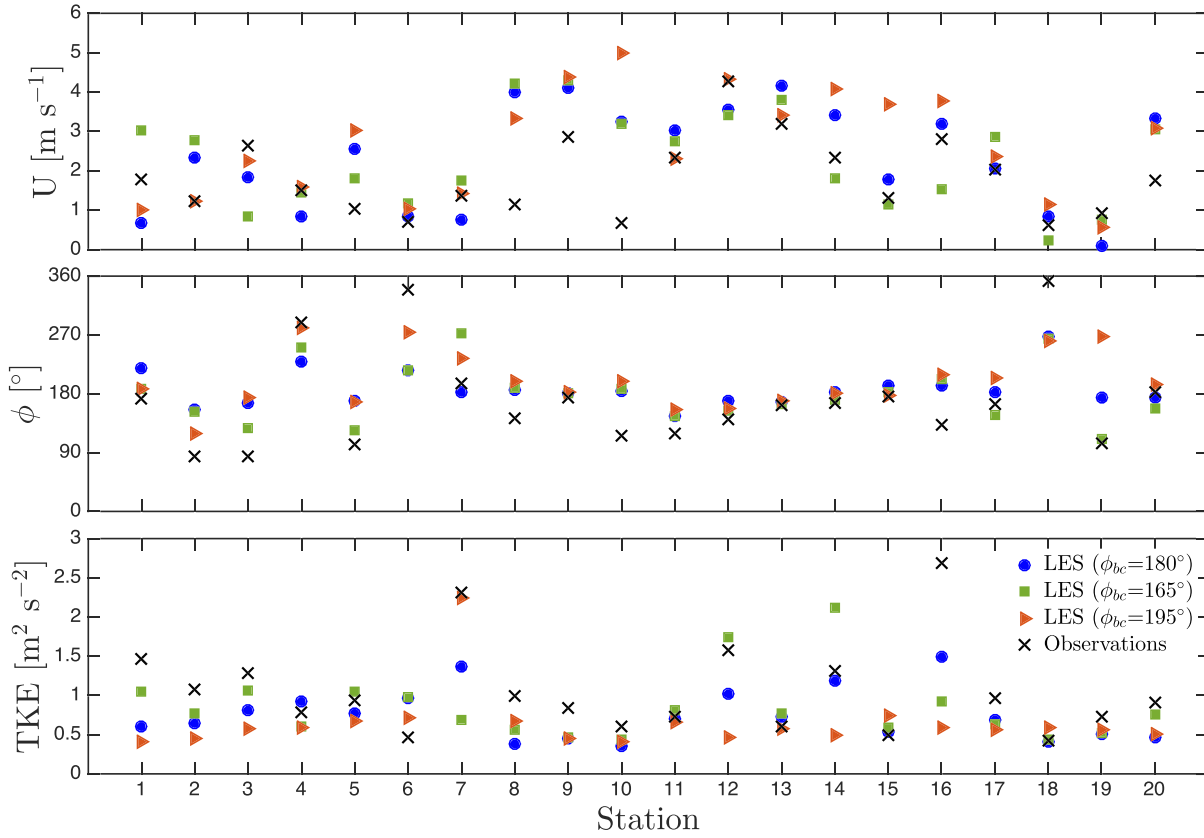


Figure 7. Comparison of simulated to observed mean wind speed, U , wind direction, ϕ , and resolved turbulence kinetic energy, TKE, during the selected time period of IOP9. Different LES symbols represent a southerly inflow and $\pm 15^\circ$ scenarios.

Figure 7. This choice was partly motivated by the work from García-Sánchez et al. (2017), which found wind direction to be more dominant than wind speed and roughness length in controlling model uncertainties, as well as by the fact that the upstream observation used to calibrate inflow conditions reported $\phi = 172.1^\circ$. While some reduction of the error was experienced at S7, a systematic improvement was not achieved by varying incoming wind direction. We believe this may be partially due to the lack of explicit buildings in the upstream fetch of the domain, as well as the fact that the IBFM does not include a wall model. Nevertheless, variations in the inflow direction notably impacted the simulated wind speed and turbulence, although these were not necessarily correlated (i.e., the largest variations of wind speed and TKE did not occur at the same stations).

A more quantitative estimation of the accuracy of the simulated wind speed is included in Table 1. Several of the statistical performance metrics recommended by Hanna et al. (2004) were calculated to that end. These metrics were selected to allow comparison to all of the other LES studies of JU03 available in the literature, which also provided these same metrics. These metrics are the fraction of predictions within a factor of 2 of the observations (FAC2), the fractional bias (FB), the geometric mean bias (MG), and the normalized mean squared error (NMSE). The equations for these metrics are

$$\text{FAC2} = \text{fraction of the data satisfying } 0.5 \leq \frac{S_i}{O_i} \leq 2.0, \quad (8)$$

$$\text{FB} = \frac{\overline{O_i} - \overline{S_i}}{0.5(\overline{O_i} + \overline{S_i})}, \quad (9)$$

$$\text{MG} = \exp \left[\overline{\ln(O_i)} - \overline{\ln(S_i)} \right], \quad (10)$$

Table 1

Statistical Performance Metrics for Wind Speed, Turbulence Kinetic Energy (TKE), and SF₆ Concentration From Present LES Modeling and the Existing LES Literature on JU03 for Different Intensive Observation Periods (IOP)

Study (building method)	IOP	FAC2	FAC5	FB	MG	NMSE
Perfect model		1.00	1.00	0.00	1.00	0.00
Wind speed						
<i>Present work</i> (IBFM)	9	0.75	—	−0.24	0.89	0.34
Chan and Leach (2007) (IBFM)	3	0.74	—	−0.21	0.79	0.30
	9	0.71	—	−0.20	0.98	0.48
Neophytou et al. (2011) (solid walls)	2	0.57	—	−0.16	0.91	0.56
	8	0.67	—	−0.01	1.04	0.31
	9	0.67	—	0.12	1.14	0.26
Lundquist et al. (2012) (IBM)	3	0.71	—	−0.40	0.71	0.32
García-Sánchez et al. (2018) (solid walls)	9	0.75	—	0.23	1.50	0.14
Wiersema et al. (2020) (IBM)	3	0.73	—	−0.24	0.73	0.23
Turbulence kinetic energy						
<i>Present work</i> (IBFM)	9	0.85	—	0.34	1.35	0.31
García-Sánchez et al. (2018) (solid walls)	9	0.90	—	0.22	1.21	0.55
SF ₆ concentration						
<i>Present work</i> (IBFM)	9	0.83	1.00	0.14	1.15	0.24
Chan and Leach (2007) (IBFM)	3	—	0.42	−0.56	6.20	14.00
	9	—	0.56	−0.39	2.00	0.96
Lundquist et al. (2012) (IBM)	3	—	0.53	−1.54	0.32	28.70
Wyszogrodzki et al. (2012) (IBM)	6	0.27	0.59	−0.15	1.28	4.48
	8	0.36	0.64	−0.17	1.19	11.29
Wiersema et al. (2020) (IBM)	3	0.56	0.76	−0.22	0.83	—

Note. The metric values corresponding to a perfect model (zero error) are included for reference.

$$\text{NMSE} = \frac{\overline{(O_i - S_i)^2}}{\overline{O_i S_i}}, \quad (11)$$

where the overbars denote averaging over all the stations, and O_i and S_i are the observed and simulated values at a given station, respectively. Our results are within the distribution of metric values of the different models, and fall within the acceptance limits proposed by Hanna et al. (2004). The present results have the highest FAC2 for wind speed (=0.75), together with the modeling from García-Sánchez et al. (2018). In general, all models share a consistent negative fractional bias (i.e., trend of the simulations to over predict the observed winds). This can be partly attributed to subgrid scale obstacles like bushes, trees and traffic lights and signals that are not included in the simulations. Moreover, the skill of the same model shows significant variability among different IOPs. This can be clearly seen from the NMSE for Chan and Leach (2007) and Neophytou et al. (2011), with the latter exhibiting more than a factor of 2 variability on that metric among IOPs despite using the same building layout and grid spacing. This points to the importance of realistic coupling to dynamic weather conditions in order to reproduce real-world conditions (e.g., Muñoz-Esparza et al., 2017; Wiersema et al., 2020; Wyszogrodzki et al., 2012). Note that for the IOP9 period we simulated here, a cooling rate of $\approx 1 \text{ K h}^{-1}$ was reported at the incoming 30-m height station used for inflow condition reference. We performed an additional run imposing a surface cooling rate of 1 K h^{-1} in the LAD to investigate this aspect, albeit using the same neutrally stratified mean profiles as lateral boundary conditions. The application of a cooling rate did not make a noticeable difference with respect to the reference simulation by itself (not shown). However, the lateral boundary conditions were kept as in the reference case, so we expect that a more sophisticated lateral forcing consistent with the surface cooling, as well as other enhancements such as incorporation of both a wall model and a building energy model will result in significant improvement.

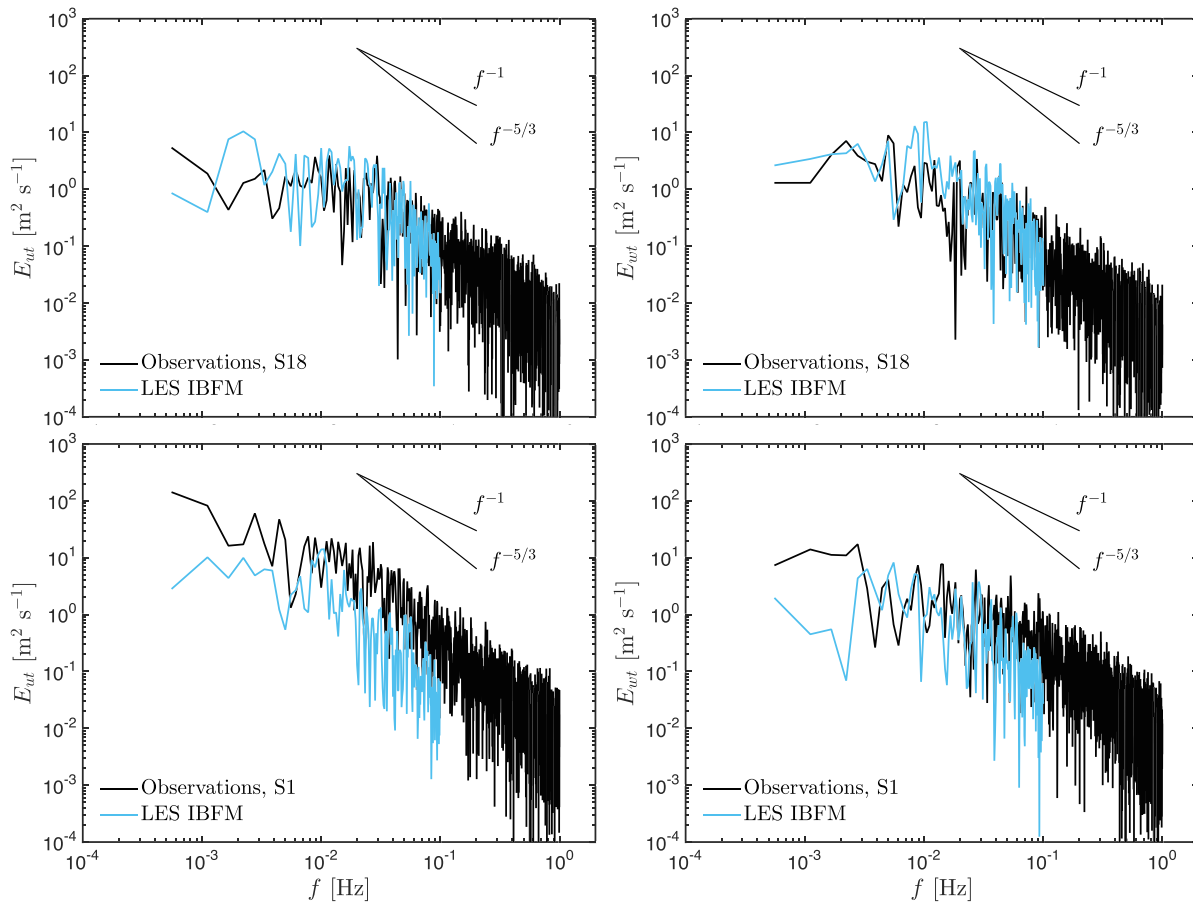


Figure 8. Spectral density of horizontal (left panels) and vertical velocity fluctuations (right panels) as a function of frequency for the sonic anemometer observations and LES IBFM results at Stations 18 (top panels) and 1 (bottom panels) during IOP9 (0400–0430 UTC on 27 July). Solid lines correspond to Kolmogorov’s $-5/3$ theoretical inertial range slope for three-dimensional isotropic turbulence and -1 slope associated with turbulence production. LES IBFM results are lowpass filtered to the effective resolution ($f_c = 0.1$ Hz) and sonic anemometer observations are clipped to $f \leq 1$ Hz for visualization purposes.

One of the advantages of LES of urban canopies versus other more simplified types of models is its superior performance in predicting turbulence related quantities (e.g., García-Sánchez et al., 2018). Moreover, LES has the advantage that is inherently unsteady and thus reproduces the spectral distribution of eddy motions that can be resolved by a given grid spacing. An example of that is depicted in Figure 8, where the spectral density distributions for two of the stations, S18 and S1, are presented. The horizontal and vertical velocity fluctuations are included, since a significant anisotropic component is present in urban canopy flows over a wide range of frequencies (wavenumbers). Both the sonic anemometer and LES IBFM results were low pass filtered to derive TKE, in order to account for the finite grid spacing of the model and its effective resolution (e.g., Skamarock, 2004) and therefore allow comparison of model and observations in a consistent manner. A cutoff frequency of $f_c = 0.1$ Hz was employed, using a tenth-order digital Chebyshev filter to effectively remove higher frequency energy content without altering lower frequencies.

Figure 8 shows the lowpass filtered LES IBFM spectra, while the observations are displayed in its original form (no filter) up to a frequency of 1 Hz. For Station S18, located on the lee side of the Cox Convention Center, a very good match between model results and observations is found for both U and w energy content, which resulted in a very accurate prediction of TKE at that station (see Figure 7). For the frequency range resolved by the model, the slope of the spectra is closer to -1 , indicating the predominance of turbulence production as a combined effect from the presence of the nearby buildings and the proximity to the ground ($z = 8$ m). Observations reveal a transition toward a $-5/3$ slope at higher frequencies. In contrast, and although the slope of the energy distribution is well captured by the model at Station S1, there is a systematic decrease in magnitude of the velocity fluctuations, more pronounced in the horizontal direction. Station S1 is located on a less densely built up area, especially toward the north and east regions of the

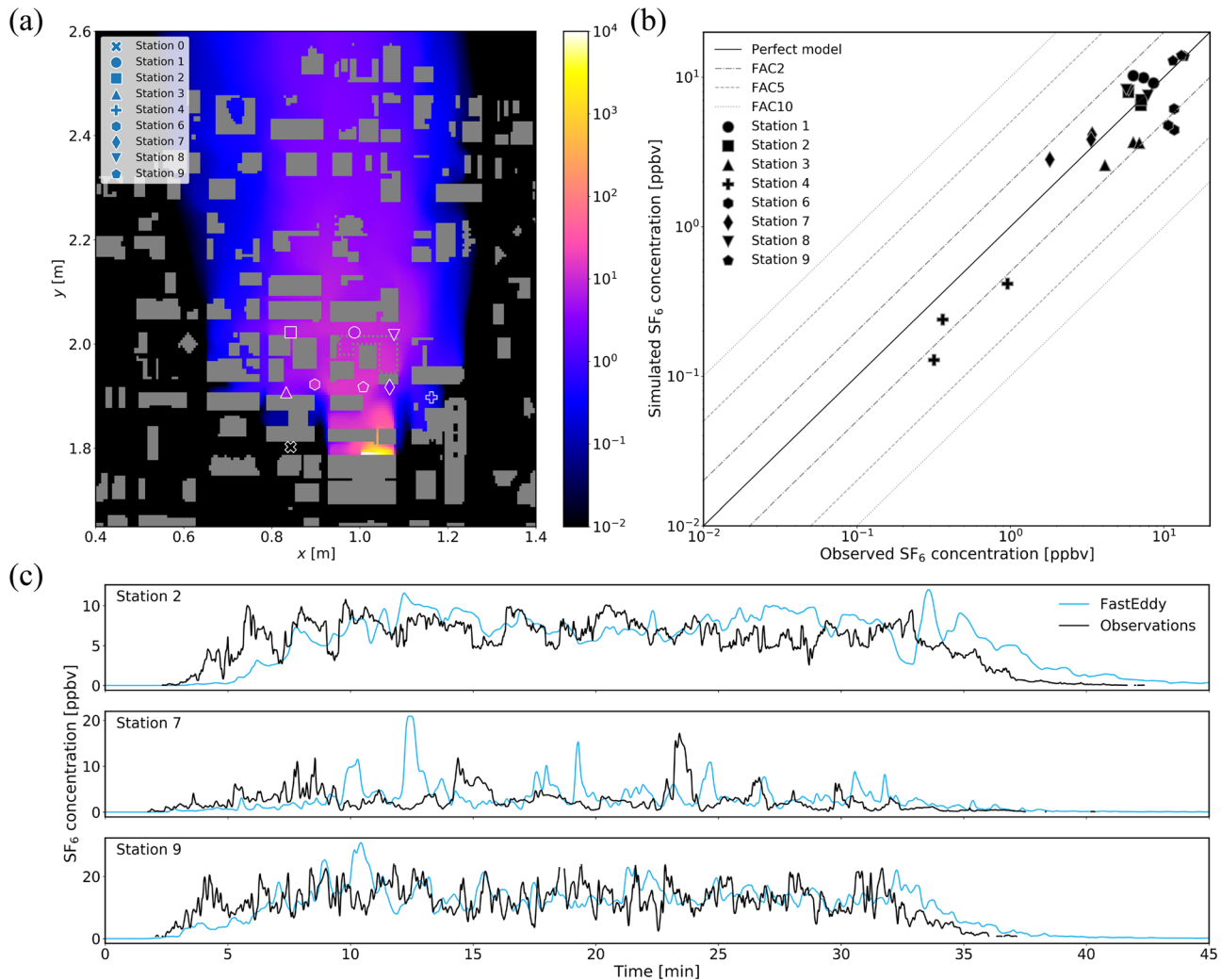


Figure 9. SF₆ concentration results for the continuous release simulation. (a) Contours of mean simulated SF₆ concentration at $z = 2.5$ m and reported ARLFRD tracer gas analyzer concentrations averaged over the 30-min continuous release period (ppbv). (b) Scatter plot of observed versus simulated SF₆ concentrations at each of the stations and averaged over 10-min intervals. Solid lines indicate one-to-one correlation (perfect model, in black), together with FAC2, FAC5, and FAC10 (gray dashed lines). (c) Time series of SF₆ concentration at Stations 2, 7, and 9 from the fast-response tracer analyzers (2 Hz) and the LES model (1 Hz).

station, resulting in spanwise dominant motions that have reduced vorticity. We hypothesize that the omission of trees and bushes in the model, together with a less dense building layout, is responsible for the turbulence underprediction at that location. The overall performance in predicting TKE is reasonable, given all the challenges already mentioned, and is essentially the same as the one by García-Sánchez et al. (2018) using a solid wall approach (body-fitted grid) to model the buildings (see Table 1), in both cases finding a positive fractional bias (underprediction) of TKE, attributed to the reasons already discussed.

Finally, we demonstrate FastEddy's transport and dispersion capabilities alongside the IBFM by simulating one of the continuous releases during IOP9. The selected scenario corresponds to a release of sulfur hexafluoride (SF₆) at a constant rate of 2.0 g s^{-1} over a 30-min time interval. For the SF₆ transport and dispersion simulation we rotated the inflow wind profile at $\phi = 172.5^\circ$ to better match the observed wind direction, indicated to be the dominant boundary condition parameter in the urban dispersion uncertainty quantification analysis by García-Sánchez et al. (2017). SF₆ is treated as a passive tracer given the small density ratio compared to the air, of approximately 0.006. Figure 9a shows contours of time-averaged simulated SF₆ concentration at $z = 2.5$ m, together with the PIGS concentration observations (in parts per billion by volume, ppbv). The spatial distribution of the time-averaged simulated SF₆ concentration field agrees very well with the concentration measurements from the observational network. Quantification of the skill of the model

in reproducing the observed SF₆ concentrations over the time of the release is provided by the scatter plot of PIGS observations vs simulation results presented in Figure 9b. There, 10-min nonoverlapping averages are considered, to better account for the transient nature of these observations, while not being too short to preclude a meaningful comparison due to sampling issues in the presence of atmospheric turbulence. The simulation results are highly correlated with the observations across the entire range of concentrations and disparate station locations. All instances fall close to the one-to-one line, indicating a high accuracy of this urban transport and dispersion scenario as simulated by our model. In particular, the majority of the model results fall within a factor of 2 from the observations, with a corresponding FAC2 of 0.83. As seen from Table 1, our model has considerably larger FAC2 and FAC5 than any of the other LES model results in the published literature, and does exhibit an excellent statistical performance when considering all of the other metrics. Note that in all the published OKC LES studies, including ours, the skill of the numerical solution is subject to the specific choice of forcing conditions and physics simplifications. Therefore, and given that only one simulation is performed per IOP in these studies, the statistical significance of the assessment metrics may not be as high as desired. Nonetheless, it is the most rigorous exercise that can be performed to put our results in the context of the published literature. Also, we found that the IBFM-induced leakage effect of SF₆ inside buildings was marginal (less than 5% of the instantaneous total accumulated amount), further validating the applicability of the IBFM for simulating flow and dispersion in urban environments. If simulations are performed over significantly larger times, and releases are constant, this error can potentially increase.

Large-eddy simulation's ability to model the unsteady effects of turbulence (both ambient atmospheric turbulence and urban environment induced) is the primary advantage over simpler steady-state dispersion models. This capability is illustrated by the time series of SF₆ concentration at three of the PIGS station locations in Figure 9c, where SF₆ arrival and postrelease decay times are well captured by our model. While LES cannot perfectly replicate the presence of a particular eddy at a specific time, it does realistically capture the influence of turbulent eddies in a statistical sense. This can also be observed from the time series, which clearly depict similar amplitude and variability characteristics in both the simulation and the observations of unique time series signatures of turbulent eddies impacting each location. For example, the simulated concentration at Station 2 reports a local maximum at $t \approx 12.5$ min, which is of very similar structure to the one observed at $t \approx 23$ min. These events are preceded in both cases by drops in SF₆ concentration at Station 9, indicative of unsteady local street canyon effects that are captured by the LES simulations with a high degree of fidelity.

In addition, it is worth remarking that the FastEddy model provides an efficient research tool for scientific advancements in the realm of urban flow modeling. One of our 2-m OKC simulations requires 12.8 h on an 8 NVIDIA Volta V100 GPUs node. This is considerably more efficient than typical state-of-the-art CPU-based codes, like the example in García-Sánchez et al. (2018), which instead required 340,000 CPU hours on a supercomputer to perform a similar simulation (340 h using 1,000 CPUs). This is a significant speed up that can facilitate scientific investigations, efficiently employing LES at unprecedentedly fine grid spacings as the ones required for building-resolving urban simulations.

5. Conclusions

Fine-scale weather modeling in urban environments is critical for many applications. In this manuscript, we have implemented and verified/validated an immersed body force method (IBFM) to explicitly represent building effects in the resident-GPU FastEddy model. The proposed IBFM is an extension of the work by Chan and Leach (2007), which is based on the use of large drag forces that mimic the presence of solid bodies in the velocity field. Herein, we have proposed two modifications to the IBFM that make it applicable to a broad range of scales (from laboratory experiments to atmospheric scale urban environments) and to be able to control thermal effects by additional terms to the thermodynamic equations. The extended IBFM has been verified to recover nearly zero velocities inside the buildings as well as maintaining an imposed building surface temperature in the presence of a surface heat flux. Excellent validation for the flow over a staggered array of cubes at wind tunnel scale was achieved, demonstrating the appropriateness of the proposed scale-independent IBFM. Finally, simulation of the flow, turbulence and dispersion during one of the IOPs of the Oklahoma Joint Urban field campaign in 2003 established that the present LES IBFM is as accurate as other existing LES models with urban capabilities.

The extended IBFM has the advantage of being computationally very efficient, while retaining the ability of immersed boundary methods to use structured grids (versus the body-fitted grids employed by the solid wall approach). Another advantage of the IBFM is its potential to be easily extended to model canopy flows. Given its similarity to a canopy-drag term, the same IBFM can be used to simultaneously simulate buildings and canopies with the incorporation of two additional static arrays providing spatial information of canopy drag coefficient and leaf area density. The current IBFM is essentially a low-Reynolds number approach, imposing a no-slip velocity type of boundary condition at the building walls. We plan to extend the IBFM to incorporate a rough-wall model, which is expected to improve results in regions close to the building walls. To that end, we plan to implement an approach based on a canopy formulation to deal with the wall model, similar to Anderson (2013), which would additionally allow representation of flows over complex terrain. In addition, our proposed extension that allows controlling of building temperatures is a desired feature to enable coupling to building energy models (e.g., Nazarian et al., 2018; Park et al., 2012; Yaghoobian et al., 2014). We are currently working on the coupling of FastEddy to mesoscale models in order to account for more realistic heterogeneous and time-varying atmospheric forcing conditions, and in turn improve the predictions at urban scale (e.g., Wiersema et al., 2020; Wyszogrodzki et al., 2012). All these features of the IBFM, combined with the GPU-enabled accelerated LES modeling in FastEddy, will facilitate a path toward realistic street-scale operational weather forecasting in the near future.

Data Availability Statement

Processed model output relevant to this study is publicly available via Zenodo (<https://doi.org/10.5281/zenodo.4124164>).

Acknowledgments

This research was funded by the 2018 NCAR Research Applications Laboratory (RAL) Opportunity Award: “Microscale Modeling Capabilities for Flow and Turbulence Prediction in Urban Environments.” The simulations and results presented here were performed through the Cheyenne and Casper computational resources (doi:10.5065/D6RX99HX) at the NCAR-Wyoming Supercomputing Center provided by the National Science Foundation and the State of Wyoming and supported by NCAR’s Computational and Information Systems Laboratory.

References

Allwine, K. J., & Flaherty, J. E. (2006). Urban dispersion program MSG05 field study: Summary of tracer and meteorological measurements (Tech. Rep. PNNL-15969). Richland, WA (United States): Pacific Northwest National Laboratory (PNNL).

Anderson, W. (2013). An immersed boundary method wall model for high-Reynolds-number channel flow over complex topography. *International Journal for Numerical Methods in Fluids*, 71(12), 1588–1608.

Auguste, F., Réa, G., Paoli, R., Lac, C., Masson, V., & Cariolle, D. (2019). Implementation of an immersed boundary method in the Meso-NH v5. 2 model: Applications to an idealized urban environment. *Geoscientific Model Development*, 12(6), 2607–2633.

Bao, J., Chow, F. K., & Lundquist, K. A. (2018). Large-eddy simulation over complex terrain using an improved immersed boundary method in the weather research and forecasting model. *Monthly Weather Review*, 146(9), 2781–2797.

Blocken, B. (2018). LES over RANS in building simulation for outdoor and indoor applications: A foregone conclusion? *Building Simulation*, 11(5), 821–870.

Castro, I. P., Cheng, H., & Reynolds, R. (2006). Turbulence over urban-type roughness: Deductions from wind-tunnel measurements. *Boundary-Layer Meteorology*, 118(1), 109–131.

Chan, S. T., & Leach, M. J. (2007). A validation of FEM3MP with Joint Urban 2003 data. *Journal of Applied Meteorology and Climatology*, 46(12), 2127–2146.

Cheng, W.-C., & Porté-Agel, F. (2015). Adjustment of turbulent boundary-layer flow to idealized urban surfaces: A large-eddy simulation study. *Boundary-Layer Meteorology*, 155(2), 249–270.

Coccal, O., Thomas, T., Castro, I., & Belcher, S. (2006). Mean flow and turbulence statistics over groups of urban-like cubical obstacles. *Boundary-Layer Meteorology*, 121(3), 491–519.

García-Sánchez, C., van Beeck, J., & Gorlé, C. (2018). Predictive large eddy simulations for urban flows: Challenges and opportunities. *Building and Environment*, 139, 146–156.

García-Sánchez, C., Van Tendeloo, G., & Gorlé, C. (2017). Quantifying inflow uncertainties in RANS simulations of urban pollutant dispersion. *Atmospheric Environment*, 161, 263–273.

Gorlé, C., van Beeck, J., & Rambaud, P. (2010). Dispersion in the wake of a rectangular building: Validation of two Reynolds-averaged Navier–Stokes modelling approaches. *Boundary-Layer Meteorology*, 137, 115–133.

Hanna, S. R., Hansen, O. R., & Dharmavaram, S. (2004). FLACS CFD air quality model performance evaluation with Kit Fox, MUST, Prairie Grass, and EMU observations. *Atmospheric Environment*, 38(28), 4675–4687.

Iaccarino, G., & Verzicco, R. (2003). Immersed boundary technique for turbulent flow simulations. *Applied Mechanics Reviews*, 56(3), 331–347.

Jähn, M., Muñoz-Esparza, D., Chouza, F., Reitebuch, O., Knoth, O., Haarig, M., & Ansmann, A. (2016). Investigations of boundary layer structure, cloud characteristics and vertical mixing of aerosols at Barbados with large eddy simulations. *Atmospheric Chemistry & Physics*, 16(2), 651–674.

Jiang, P., Wen, Z., Sha, W., & Chen, G. (2017). Interaction between turbulent flow and sea breeze front over urban-like coast in large-eddy simulation. *Journal of Geophysical Research: Atmospheres*, 122, 5298–5315. <https://doi.org/10.1002/2016JD026247>

Kanda, M. (2006). Large-eddy simulations on the effects of surface geometry of building arrays on turbulent organized structures. *Boundary-Layer Meteorology*, 118(1), 151–168.

Lee, G.-J., Muñoz-Esparza, D., Yi, C., & Choe, H. J. (2019). Application of the cell perturbation method to large-eddy simulations of a real urban area. *Journal of Applied Meteorology and Climatology*, 58(5), 1125–1139.

Lenz, S., Schoenherr, M., Geier, M., Krafczyk, M., Pasquali, A., Christen, A., & Giometto, M. (2019). Towards real-time simulation of turbulent air flow over a resolved urban canopy using the cumulant lattice Boltzmann method on a GPGPU. *Journal of Wind Engineering and Industrial Aerodynamics*, 189, 151–162.

- Letzel, M. O., Krane, M., & Raasch, S. (2008). High resolution urban large-eddy simulation studies from street canyon to neighbourhood scale. *Atmospheric Environment*, *42*(38), 8770–8784.
- Li, Q., Bou-Zeid, E., Anderson, W., Grimmond, S., & Hultmark, M. (2016). Quality and reliability of LES of convective scalar transfer at high Reynolds numbers. *International Journal of Heat and Mass Transfer*, *102*, 959–970.
- Lilly, D. K. (1966). On the application of the eddy viscosity concept in the inertial sub-range of turbulence. National Center for Atmospheric Research, NCAR Manuscript No. 123 19 pp.
- Lilly, D. K. (1967). The representation of small scale turbulence in numerical simulation experiments. In *IBM Scientific Computing Symposium on Environmental Sciences* (pp. 195–210). White Plains.
- Lundquist, K. A., Chow, F. K., & Lundquist, J. K. (2012). An immersed boundary method enabling large-eddy simulations of flow over complex terrain in the WRF model. *Monthly Weather Review*, *140*(12), 3936–3955.
- Maronga, B., Gryscha, M., Heinze, R., Hoffmann, F., Kanani-Sühring, F., Keck, M., et al. (2015). The Parallelized Large-eddy Simulation Model (PALM) Version 4.0 for atmospheric and oceanic flows: Model formulation, recent developments, and future perspectives. *Geoscientific Model Development Discussions* *8* (2015), Nr. 2, S. 1539–1637, 8, 2515–2551.
- Mirocha, J., Kirkil, G., Bou-Zeid, E., Chow, F. K., & Kosović, B. (2013). Transition and equilibration of neutral atmospheric boundary layer flow in one-way nested large-eddy simulations using the Weather Research and Forecasting model. *Monthly Weather Review*, *141*(3), 918–940.
- Mittal, R., & Iaccarino, G. (2005). Immersed boundary methods. *Annual Review of Fluid Mechanics*, *37*, 239–261.
- Muñoz-Esparza, D., Kosović, B., García-Sánchez, C., & van Beeck, J. (2014). Nesting turbulence in an offshore convective boundary layer using large-eddy simulations. *Boundary-Layer Meteorology*, *151*(3), 453–478.
- Muñoz-Esparza, D., Kosović, B., Mirocha, J., & van Beeck, J. (2014). Bridging the transition from mesoscale to microscale turbulence in numerical weather prediction models. *Boundary-Layer Meteorology*, *153*(3), 409–440.
- Muñoz-Esparza, D., Kosović, B., van Beeck, J., & Mirocha, J. (2015). A stochastic perturbation method to generate inflow turbulence in large-eddy simulation models: Application to neutrally stratified atmospheric boundary layers. *Physics of Fluids (1994-present)*, *27*(3), 035102.
- Muñoz-Esparza, D., Lundquist, J. K., Sauer, J. A., Kosović, B., & Linn, R. R. (2017). Coupled mesoscale-LES modeling of a diurnal cycle during the CWEX-13 field campaign: From weather to boundary-layer eddies. *Journal of Advances in Modeling Earth Systems*, *9*, 1572–1594. <https://doi.org/10.1002/2017MS000960>
- Nazarian, N., Martilli, A., Norford, L., & Kleissl, J. (2018). Impacts of realistic urban heating. Part II: Air quality and city breathability. *Boundary-Layer Meteorology*, *168*(2), 321–341.
- Neophytou, M., Gowardhan, A., & Brown, M. (2011). An inter-comparison of three urban wind models using Oklahoma City Joint Urban 2003 wind field measurements. *Journal of Wind Engineering and Industrial Aerodynamics*, *99*(4), 357–368.
- Park, S.-B., Baik, J.-J., & Lee, S.-H. (2015). Impacts of mesoscale wind on turbulent flow and ventilation in a densely built-up urban area. *Journal of Applied Meteorology and Climatology*, *54*(4), 811–824.
- Park, S.-B., Baik, J.-J., Raasch, S., & Letzel, M. O. (2012). A large-eddy simulation study of thermal effects on turbulent flow and dispersion in and above a street canyon. *Journal of Applied Meteorology and Climatology*, *51*(5), 829–841.
- Sauer, J. A., & Muñoz-Esparza, D. (2020). The FastEddy[®] resident-GPU accelerated large-eddy simulation framework: Model formulation, dynamical-core validation and performance benchmarks. *Journal of Advances in Modeling Earth Systems*, *12*. <https://doi.org/10.1029/2020MS002100>
- Schalkwijk, J., Griffith, E. J., Post, F. H., & Jonker, H. J. (2012). High-performance simulations of turbulent clouds on a desktop PC: Exploiting the GPU. *Bulletin of the American Meteorological Society*, *93*(3), 307–314.
- Senocak, I., Ackerman, A., Mansour, N., & Stevens, D. (2004). Topography modeling in atmospheric flows using the immersed boundary method. *Annual Research Briefs, Center for Turbulence Research*, 331–341.
- Shin, H. H., Muñoz-Esparza, D., Sauer, J. A., & Stenier, M. (2020). Large-eddy simulations of flow around isolated buildings immersed in the atmospheric boundary layer under varying stability conditions. *Journal of the Atmospheric Sciences (conditionally accepted)*.
- Skamarock, W. C. (2004). Evaluating mesoscale NWP models using kinetic energy spectra. *Monthly Weather Review*, *132*(12), 3019–3032.
- Smolarkiewicz, P. K., Sharman, R., Weil, J., Perry, S. G., Heist, D., & Bowker, G. (2007). Building resolving large-eddy simulations and comparison with wind tunnel experiments. *Journal of Computational Physics*, *227*(1), 633–653.
- Thibault, J., & Senocak, I. (2009). CUDA implementation of a Navier-Stokes solver on multi-GPU desktop platforms for incompressible flows. In *47th AIAA Aerospace Sciences Meeting Including the New Horizons Forum and Aerospace Exposition* (pp. 758). Orlando, Florida: AIAA.
- Tomas, J., Pourquie, M., & Jonker, H. (2016). Stable stratification effects on flow and pollutant dispersion in boundary layers entering a generic urban environment. *Boundary-Layer Meteorology*, *159*(2), 221–239.
- van Heerwaarden, C. C., Van Stratum, B. J., Heus, T., Gibbs, J. A., Fedorovich, E., & Mellado, J. P. (2017). MicroHH 1.0: A computational fluid dynamics code for direct numerical simulation and large-eddy simulation of atmospheric boundary layer flows. *Geoscientific Model Development*, *10*(8), 3145–3165.
- Vanella, M., Piomelli, U., & Balaras, E. (2008). Effect of grid discontinuities on large-eddy simulation statistics and flow fields. *Journal of Turbulence*, *9*(32), 1–23.
- Wicker, L. J., & Skamarock, W. C. (2002). Time-splitting methods for elastic models using forward time schemes. *Monthly Weather Review*, *130*(8), 2088–2097.
- Wiersema, D. J., Lundquist, K. A., & Chow, F. K. (2020). Mesoscale to microscale simulations over complex terrain with the immersed boundary method in the weather research and forecasting model. *Monthly Weather Review*, *148*(2), 577–595.
- Wyszogrodzki, A. A., Miao, S., & Chen, F. (2012). Evaluation of the coupling between mesoscale-WRF and LES-EULAG models for simulating fine-scale urban dispersion. *Atmospheric Research*, *118*, 324–345.
- Yaghoobian, N., Kleissl, J., & Tha P. U. K. (2014). An improved three-dimensional simulation of the diurnally varying street-canyon flow. *Boundary-Layer Meteorology*, *153*(2), 251–276.
- Yamada, T. (1982). A numerical model study of turbulent airflow in and above a forest canopy. *Journal of the Meteorological Society of Japan. Ser. II*, *60*(1), 439–454.